nature communications

Article

https://doi.org/10.1038/s41467-022-33053-x

Hardware implementation of Bayesian network based on two-dimensional memtransistors

Received: 13 January 2022

Accepted: 31 August 2022

Published online: 23 September 2022

Yikai Zheng[1], Harikrishnan Ravichandran[1], Thomas F. Schranghamer[1], Nicholas Trainor[2,3], Joan M. Redwing[2,3] & Saptarshi Das[1,2,3,4] ✉

Bayesian networks (BNs) find widespread application in many real-world probabilistic problems including diagnostics, forecasting, computer vision, etc. The basic computing primitive for BNs is a stochastic bit (s-bit) generator that can control the probability of obtaining '1' in a binary bit-stream. While silicon-based complementary metal-oxide-semiconductor (CMOS) technology can be used for hardware implementation of BNs, the lack of inherent stochasticity makes it area and energy inefficient. On the other hand, memristors and spintronic devices offer inherent stochasticity but lack computing ability beyond simple vector matrix multiplication due to their two-terminal nature and rely on extensive CMOS peripherals for BN implementation, which limits area and energy efficiency. Here, we circumvent these challenges by introducing a hardware platform based on 2D memtransistors. First, we experimentally demonstrate a low-power and compact s-bit generator circuit that exploits cycle-to-cycle fluctuation in the post-programmed conductance state of 2D memtransistors. Next, the s-bit generators are monolithically integrated with 2D memtransistor-based logic gates to implement BNs. Our findings highlight the potential for 2D memtransistor-based integrated circuits for non-von Neumann computing applications.

The concept of a Bayesian network (BN) is deep rooted within natural intelligence. Animals gather information from their surroundings with the help of their sensory organs and process this information using their brain to make decisions, enabling their survival. However, gathering accurate information is often very difficult in practice either due to the limitations of sensory organs or due to noisy environment. For example, visual cues are an unreliable source of information for freshwater fish like the rainbow trout to identify the presence of a predator. In contrast, chemical cues released into the water from an injured fish are more reliable indicators of a predatory event[1]. The decision to invoke an alarm response, therefore, depends on how the brain processes the visual and chemical cues based on their relative probability of success from prior experiences. While the neural basis of such computations is relatively unknown, the mathematical construct is represented using a BN with theoretical foundation in Bayes' theorem.

A BN is a probabilistic graphic network used to estimate and infer the probability of interdependent events[2]. Figure 1a shows the basic building block of a BN, comprising a parent node, A, a child node, B, and an edge connecting the two. Each node represents an event, e.g., the presence of a chemical cue (A) and the presence of a predator (B), and the connection represents how two events are mutually dependent. The dependence is provided in a conditional probability table (CPT) which contains the conditional probability (likelihood) values $P(B/A)$ and $P(B/A^c)$, where A^c is the complement of the event A. In the present example, these represent the likelihood of the presence of a

[1]Engineering Science and Mechanics, Penn State University, University Park 16802 PA, USA. [2]Materials Science and Engineering, Penn State University, University Park 16802 PA, USA. [3]Materials Research Institute, Penn State University, University Park 16802 PA, USA. [4]Electrical Engineering and Computer Science, Penn State University, University Park 16802 PA, USA. ✉e-mail: sud70@psu.edu

https://doi.org/10.1038/s41467-022-33053-x

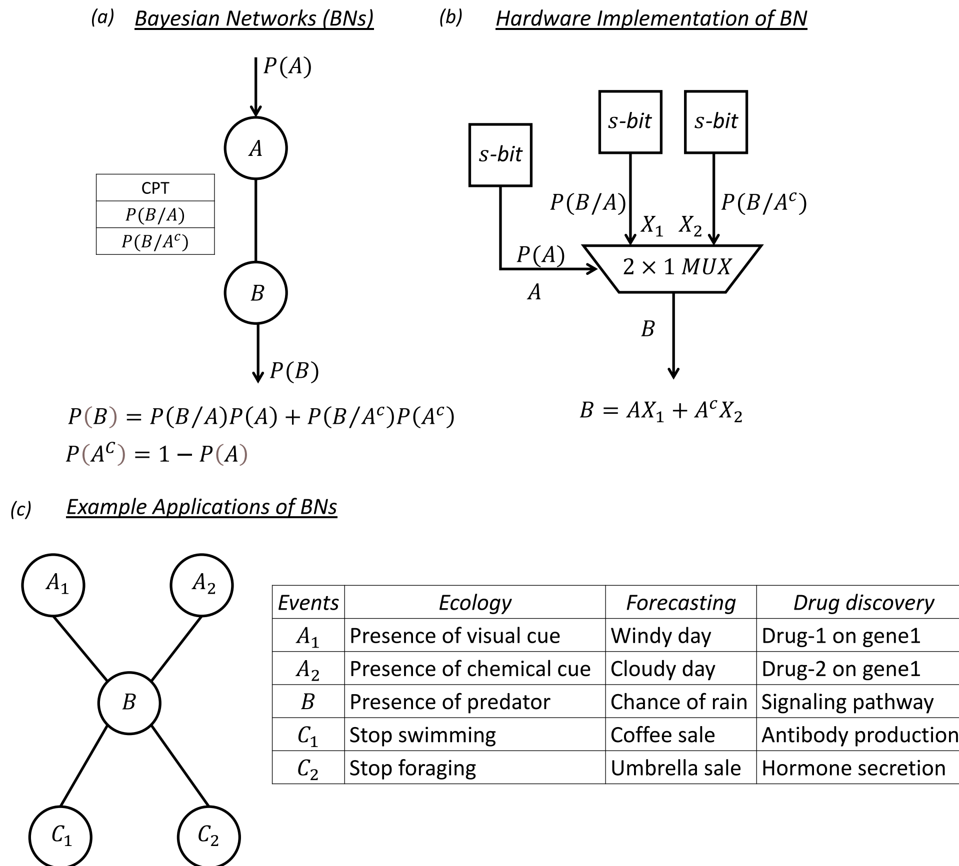

Events	Ecology	Forecasting	Drug discovery
A_1	Presence of visual cue	Windy day	Drug-1 on gene1
A_2	Presence of chemical cue	Cloudy day	Drug-2 on gene1
B	Presence of predator	Chance of rain	Signaling pathway
C_1	Stop swimming	Coffee sale	Antibody production
C_2	Stop foraging	Umbrella sale	Hormone secretion

Fig. 1 | Bayesian networks (BNs). a Schematic of the basic building block of a BN, comprising a parent node, A, a child node, B, and an edge connecting the two. Each node represents an event, and the connection represents how two events are mutually dependent. The dependence is provided in a conditional probability table (CPT), which contains the conditional probability (likelihood) values $P(B/A)$ and $P(B/A^c)$, where A^c is the complement of the event. Knowing the probability of occurrence for event A, i.e., $P(A)$, the marginal probability of occurrence of event B, i.e., $P(B)$, can be evaluated using Bayes' theorem. **b** Hardware implementation of the 2-node BN in (**a**) using three stochastic bit (s-bit) generators and one 2×1 multiplexer (MUX) circuit. **c** Examples of BN architecture that represent real-life situations from ecology to forecasting and drug discovery, highlighting its usefulness in decision making.

predator when a chemical cue is present (A) or absent (A^c), respectively. When the probability of occurrence for event A, i.e., $P(A)$, is known, the marginal probability of occurrence of event B, i.e., $P(B)$, can be evaluated using Bayes' theorem following Eq. 1.

$$P(B)=P(B/A)P(A)+P(B/A^c)P(A^c)=P(B/A)P(A)+P(B/A^c)[1-P(A)] \quad (1)$$

$$P(A)+P\left(A^C\right)=1 \quad (2)$$

In a generic BN, a child node can have multiple parent nodes, and a parent node can have multiple children. For example, Supplementary Fig. S1a shows a BN where the child node, B, is connected to 2 parent nodes, A_1 and A_2. Note that the CPT in this instance contains N = 4 entries, which are the conditional probability (likelihood) for the occurrence of event B under all possible combinations of the occurrence of events A_1 and A_2. Similarly, Supplementary Fig. S1b shows a BN where the parent node, A, is connected to 2 children, B_1 and B_2. In this case, there are 2 CPTs with N = 2 entries each.

Note that the probability estimation for a child node requires multiple arithmetic operations such as multiplication, subtraction, and addition. This makes hardware implementation of a BN using conventional silicon complementary metal-oxide-semiconductor (CMOS) technology[3,4] less attractive because 1) arithmetic operations require circuits consisting of hundreds of transistors, which have large footprints and consume a significant amount of energy, and 2) the von Neumann bottleneck necessitates storing of the CPT in the memory, which is physically separated from the arithmetic core and therefore requires frequent data shuttling between the two, further aggravating the energy burden. In contrast, even the tiniest brains with very limited numbers of neurons can perform such apparently complex computational tasks with miniscule energy expenditure. The success of biological brains in implementing BNs could lie in the inherently stochastic nature of neural computation.

Drawing inspiration from biology, stochastic computing (SC) has been explored for the hardware implementation of BNs[5]. The key difference from classical computing, where information in presented in the form of binary values (1's and 0's), is that SC encodes information using stochastic bits (s-bits) that are interpreted as probabilities that fall in the interval [0,1]. For instance, the bit-stream S = [1 0 0 1 0 1 0 0] encodes the value $P(S)$ = 3/8, i.e., the probability of finding '1' in the bit-stream S. An attractive feature of SC is that arithmetic operations can be performed using simple logic gates[6,7]. For example, the 2-node BN in Fig. 1a can be realized using a multiplexer (MUX) circuit as shown in Fig. 1b. The output, B, of a MUX with two input variables, X_1 and X_2, and a select line, A, is given by Eq. (3).

$$B=AX_1+A^cX_2 \quad (3)$$

If, instead of being digital variables, X_1, X_2, and A represent stochastic variables with $P(X_1)$, $P(X_2)$, and $P(A)$ being the respective probability of obtaining '1' in their bit-streams, then B also transforms into a

random variable whose probability is given by Eq. (4).

$$P(B)=P(A)P(X_1)+P(A^c)P(X_2) \quad (4)$$

Note that, if $P(X_1) = P(B/A)$ and $P(X_2) = P(B/A^C)$, then Eq. (4) transforms into Eq. (1). Therefore, hardware implementation of a child node with a single parent can be accomplished by using 3 s-bit generators and a 2 × 1 *MUX*. Interestingly, the *MUX* architecture can be scaled to implement any BN. For example, hardware implementation of the BN in Fig. 1a can be achieved by using 2 s-bit generators to obtain A_1 and A_2, another 4 s-bit generators to obtain the CPT, and one 4 × 1 *MUX* with 2 select lines as shown in Supplementary Fig. S1c. Similarly, Supplementary Fig. 1d shows the hardware architecture for the BN in Supplementary Fig. S1b, consisting of 1 s-bit generator to obtain A, another 4 s-bit generators to obtain the 2 CPTs, and 2 2 × 1 *MUX*s.

Note that BN architecture can be used to represent many real-life situations, as shown in Fig. 1c. For example, in the case of the rainbow trout, events A_1 and A_2 represent the presence of independent visual and chemical cues and event B represents the presence of a predator. Events C_1 and C_2, meanwhile, represent the decision taken by the rainbow trout to stop swimming and stop foraging, respectively, which are also independent of each other but depend on B. Similarly, in forecasting, events A_1 and A_2 represent the probability of a day being cloudy and windy, respectively, event B represents the probability of rain, and events C_1 and C_2 may represent the decision to purchase an umbrella or drink coffee, respectively. Finally, a third example is derived from genetics and drug discovery, where events A_1 and A_2 may represent the probability of expressing *gene* 1 and *gene* 2 when intervening with a specific drug, respectively, event B represents the activation of a critical signaling pathway, and events C_1 and C_2 represent production of specific hormones or antibodies, respectively. The above discussion exemplifies the usefulness of BNs in depicting causal relationships using acyclic graphs, which can subsequently be used to predict outcomes based on prior knowledge and likelihood. For example, to predict the relative effectiveness between drug-1 and drug-2 that influence expression for *gene* 1 and *gene* 2, respectively, the only experiments that one needs to do is to obtain respective prior results, i.e., $P(A_1)$ and $P(A_2)$. A BN can then be used to obtain marginal likelihoods, i.e., $P(C_1)$ and/or $P(C_2)$, to assess the relative effectiveness of the two drugs.

The fundamental computing primitive for the stochastic computing implementation of a BN is an s-bit generator, which allows control of the output probability of obtaining '1' in a given bit-stream. So far, probabilistic CMOS[8], field-programmable gate arrays (FPGAs)[9–11], memristors[12–14], and spintronic devices[15–21] have been successfully used for BN implementation. However, CMOS- and FPGA-based BN architectures require hundreds of transistors to generate s-bits, which limits their area and energy efficiency[22–27]. In contrast, memristors offer inherent stochasticity in their switching dynamics, which can be exploited to obtain random bits. However, memristor-based BN architectures heavily rely on CMOS peripherals to translate random bits into s-bits and for subsequent logic operations using those s-bits. Recently, spintronic devices such as magnetic random access memory (MRAM)[28] and magnetic tunnel junctions (MTJs)[29–31] have shown potential for BN implementation since s-bits can be obtained by controlling the probability of spin-flip through externally driven current. However, temperature and supply voltage fluctuations can impact the spin-flip probability, which necessitates additional CMOS-based peripheral circuits to remove the bit-bias. In addition, spin-based devices still require CMOS-based logic circuits for BN implementation.

In this work, we demonstrate hardware implementation of a BN using a monolithic memtransistor technology based on two-dimensional (2D) semiconductors such as monolayer MoS_2. Memtransistors are three-terminal devices in which the gate terminal allows non-volatile and analog programming of the conductance states, which can then be readout by applying a source-to-drain bias. Our main contributions in this work are 1) the design of an area and energy efficient s-bit generator circuit composed of six memtransistors, allowing it to achieve a tunable probability of obtaining '1' in the bit-stream over the range [0,1], and 2) integration of s-bit generators with a 2D memtransistor-based 2×1 *MUX* that consists of three *NAND* gates and one *NOT* gate for BN implementation. In brief, we exploit the inherent stochasticity of the charge trapping and detrapping processes in the gate dielectric of the memtransistor as the source of randomness. Our in-memory computing approach based on three-terminal 2D memtransistors not only overcomes the von Neumann limitations of conventional digital CMOS, but also eliminates the need for peripherals, which is inescapable for emerging memristor- and spin-based 2-terminal stochastic devices for BN implementation.

Our choice of monolayer MoS_2 is motivated by the fact that atomically thin 2D materials are being considered for advanced technology nodes[32]. It is widely accepted that scaling silicon thickness beyond ~3–4 nm is challenging. Yet, the gate electrostatics demand aggressive reduction in the channel thickness to preserve the desired device performance for sub-10 nm technology nodes[33]. The ultimate channel thickness for a field-effect transistor (FET) would be in the sub-1 nm range, which is difficult to realize using bulk semiconductors[34], making 2D materials a natural choice for ultra-scaled FETs[35–41]. In fact, recent years have witnessed many experimental breakthroughs in the development of high-performance 2D FETs[42–45], neurosynaptic devices[46–50], and very large scale integrated (VLSI) circuits[51–54]. Similarly, theoretical calculations and quantum mechanical simulation have found that the 2D FETs can outperform CMOS HP (high performance) in both energy and delay[55–58].

Results

Fabrication and characterization of 2D memtransistors

Figure 2a, b, respectively, show the 2D schematic and optical image of a representative 2D memtransistor based on monolayer MoS_2, which is locally back-gated with sputter-deposited 40/30 nm Pt/TiN serving as the back-gate electrode with atomic layer deposition (ALD) grown 50 nm Al_2O_3 as the gate dielectric. All back-gate islands were placed on a commercially purchased SiO_2/p^{++}-Si substrate. As we will discuss later, the analog, non-volatile, and stochastic programming capability offered by the Al_2O_3/Pt/TiN gate stack is central to our BN architecture. The monolayer MoS_2 used in this work was grown using a metal-organic chemical vapor deposition (MOCVD) technique on a sapphire substrate at 950 °C[45, 59]. Use of an epitaxial substrate and elevated growth temperature ensured a uniform and high quality 2D film, which is critical for the successful demonstration of our BN architecture that involves many 2D memtransistors. For subsequent 2D memtransistor fabrication, the monolayer MoS_2 film was transferred from the growth substrate to the SiO_2/p^{++}-Si substrate with predefined islands of Al_2O_3/Pt/TiN. Details on monolayer MoS_2 synthesis, film transfer, and fabrication of the local back-gate gate islands, MoS_2 memtransistors, and BN architecture can be found in the "Methods" section as well as in the Methods sections of our recent works [45, 60–63].

The film quality and device performance were assessed using optical and electrical measurements. The Raman spectra (Supplementary Fig. S2a) obtained for a representative 2D memtransistor shows two characteristic monolayer MoS_2 peaks at 383 cm^{-1} and 404 cm^{-1} corresponding to the in-plane E_{2g} and out-of-plane A_{1g} modes, respectively, with the expected peak separation of ~20 cm^{-1} for monolayer MoS_2[64]. Similarly, the photoluminescence (PL) spectra (Supplementary Fig. S2b) shows a peak at 1.83 eV corresponding to the direct bandgap of monolayer MoS_2. The transfer characteristics, i.e., source-to-drain current (I_{DS}) versus local back-gate voltage (V_{BG}), measured using a source-to-drain bias (V_{DS}) of 1 V are shown in Fig. 2c in both linear and logarithmic scale for a representative MoS_2

https://doi.org/10.1038/s41467-022-33053-x

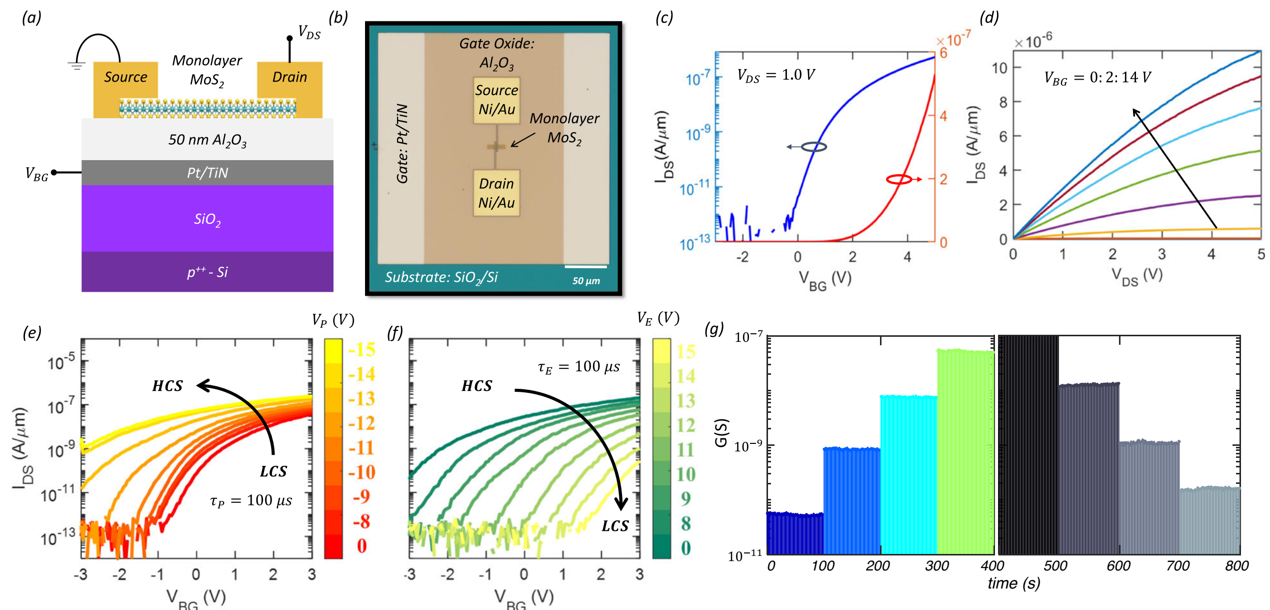

Fig. 2 | 2D memtransistors. **a** 2D schematic and **b** optical image of a representative 2D memtransistor based on monolayer MoS_2, which is locally back-gated with sputter-deposited 40/30 nm Pt/TiN serving as the back-gate electrode with atomic layer deposition (ALD) grown 50 nm Al_2O_3 as the gate dielectric. All back-gate islands were placed on a commercially purchased SiO_2/p^{++}-Si substrate. **c** Transfer characteristics, i.e., source-to-drain current (I_{DS}) versus local back-gate voltage (V_{BG}), measured at a source-to-drain bias (V_{DS}) of 1 V, in linear and logarithmic scale for a representative MoS_2 memtransistor with channel length L = 1 μm and channel width W = 5 μm. **d** Output characteristics, i.e., I_{DS} versus V_{DS}, at different V_{BG} for the same MoS_2 memtransistor. **e** Post-programmed and **f** post-erased transfer characteristics of a representative 2D memtransistor after being subjected to negative "Write" (V_P) and positive "Erase" (V_E) voltage pulses of different amplitudes applied to the local back-gate electrode, each for a duration of $\tau_{P/E}$ = 100 μs **g** Non-volatile retention for 4 representative post-programmed and post-erased conductance states (G_{MT}) over 100 s.

memtransistor with a channel length (L) of 1 μm and a channel width (W) of 5 μm. As expected, n-type transport is observed in MoS_2, which is attributed to the pinning of the metal Fermi level near the conduction band[65–67]. Nevertheless, the MoS_2 memtransistor exhibits excellent electrostatic gate control with a current on/off ratio ($r_{ON/OFF}$) > 10^5, a subthreshold slope (SS) < 400 mV/decade averaged over 3 orders of magnitude change in I_{DS}, minimal gate hysteresis when measured in air, and low gate leakage current. The threshold voltage (V_{TH}) was found to be -1.75 V extracted at an iso-current of 10 nA/μm and the electron field effect mobility (μ_{FE}) extracted from the peak transconductance was found to be 5 cm^2/V-s. Figure 2d shows the output characteristics, i.e., I_{DS} versus V_{DS}, at different V_{BG} for the same representative MoS_2 memtransistor. The on-current (I_{ON}) reached as high as ~ 11 μA/μm for an inversion carrier density of ~1×10^{12}/cm^2 at V_{DS} = 5 V. These results suggest that the monolayer MoS_2 film grown using MOCVD is of reasonably good quality, and that the memtransistor fabrication processes including the film transfer are clean and damage-free.

The post-programmed and post-erased transfer characteristics of a representative 2D memtransistor after being subjected to negative "Write" (V_P) and positive "Erase" (V_E) voltage pulses applied to the local back-gate electrode of varying amplitudes, each for a duration of $\tau_{P/E}$ = 100 μs, are shown in Fig. 2e, f, respectively. The negative and positive shift in the respective transfer characteristics can be ascribed to electron trapping and detrapping at and near the MoS_2/Al_2O_3 interface, respectively. Note that trap states can originate from defects/imperfections in the dielectric and/or adsorbed species at the 2D/dielectric interface as reported in various earlier studies[68–70]. These states can also be engineered at desired energetic locations by introducing intentional defects in the 2D channel material[51, 71]. Carrier occupancy in these trap states follow Fermi-Dirac distribution. As illustrated using the energy band diagrams in Supplementary Fig. S3, at equilibrium, i.e., in the absence of any gate bias, the trap states with energy levels above the Fermi energy (E_F) are empty, whereas the ones below E_F are filled. When the memtransistor is subjected to a negative "Write" (V_P) voltage pulse, electrons are released (detrapped) from these trap states leaving them positively charged. This leads to screening of the back-gate bias, which is reflected as shift in the threshold voltage ($\triangle V_{TH}$). Similarly, when the memtransistor is subjected to a positive "Erase" (V_E) voltage pulse, electrons are captured back (trapped) into the trap states, restoring the V_{TH}. Note that the number of electrons getting trapped/detrapped can be controlled by both the magnitude and duration of V_P and V_E, which allow us to have an analog control of the $\triangle V_{TH}$ and of the conductance state of the memtransistor.

The minimum program/erase pulse width is determined by the trapping/detrapping time constants. Supplementary Fig. S4a–d show the post-programmed and post-erased transfer characteristics of a 2D memtransistor subjected to V_P and V_E voltage pulses of different amplitudes ranging from 8 V to 15 V applied to the local back-gate electrode, each for a duration of $\tau_{P/E}$ = 100 μs, 10 μs, 1 μs, and 100 ns, respectively. Clearly, the charge trapping and detrapping processes can occur as fast as 100 ns, which is the limit set by our measurement tools, allowing further improvement in the programming speed[72, 73]. Supplementary Fig. S4e, f show the extracted shift in the threshold voltage ($\triangle V_{TH}$) as a function of $V_{P/E}$ for $\tau_{P/E}$ = 100 μs and $\tau_{P/E}$ = 100 ns, respectively. From these results, we can conclude that, for any given pulse magnitude $V_{P/E}$, $\triangle V_{TH}$ becomes smaller as $\tau_{P/E}$ becomes shorter. To retain similar $\triangle V_{TH}$ for smaller $\tau_{P/E}$, larger $V_{P/E}$ is required, which will increase the energy expenditure. Therefore, one needs to strike a balance between fast programmability and energy consumption based on the application needs.

The trapping and detrapping processes were found to be non-volatile, as shown in Fig. 2g for 4 representative post-programmed and post-erased conductance states (G_{MT}) over 100 s. We also examined long-term memory retention for the 2D memtransistors and found that states remain distinguishable even after 3 hrs. Memory retention is important to store the CPT and the memtransistors

demonstrate adequate memory performance for the hardware implementation of BNs using SC. The program/erase endurance is also important for the 2D memtransistor. Supplementary Fig. S5 shows the post-programmed and post-erased conductance states of a representative memtransistor, achieved with $V_P = -7$ V and $V_E = 10$ V using $\tau_{P/E} = 100$ ns and measured at $V_{BG} = 0$ V for up to 10^9 endurance cycles. Clearly, there is no significant change in the two states. While it is desirable to demonstrate endurance for an even higher number of cycles, note that, for the many edge applications, the current endurance results can be sufficient. For example, in weather forecasting, the BN will be used every minute rather than every microsecond; similarly, in medical diagnostics, the BN will be only used several thousand times a day to assess patients.

Programming stochasticity in 2D memtransistors and design of s-bit generator

Design of hardware for high-quality random bit generation is central to the hardware implementation of BNs. Here, we exploit the cycle-to-cycle variation in the post-programmed and post-erased conductance states (G_{MT}) of 2D memtransistors as a source of true randomness. Figure 3a shows the transfer characteristics of a representative MoS_2 memtransistor, which is measured each time after applying $V_P = -10$ V and $V_E = 10$ V for $\tau_s = 100$ μs, for a total of 100 cycles and Fig. 3b, c, respectively, show the histograms of post-programmed and post-erased G_{MT} values extracted at $V_{BG} = 0$ V. Clearly, the G_{MT} values follow Gaussian random distributions. The cycle-to-cycle variation in program/erase processes is a direct consequence of the stochastic nature of charge trapping and detrapping observed in most semiconductor/dielectric interfaces[74–76]. In the simple two-state model, a trap state can be electrically neutral or charged, and it can transition between the two states even under equilibrium condition with transition times exponentially distributed. In other words, the state transition dynamics for traps follows the classic Markovian process[77,78]. In ultra-scaled metal-oxide-semiconductor field effect transistors (MOSFETs) such stochastic state transitions lead to random telegraph noise (RTN). Metastable states are also often involved in the trapping/detrapping processes, making the transition dynamic more complex, rich, and, at the same time, introducing an additional source of randomness[79]. While RTN is not observed in our relatively large area memtransistors, the stochasticity of trapping/detrapping processes manifest during the program/erase operations, thus leading to the cycle-to-cycle variation in $\triangle V_{TH}$.

To translate the stochastic conductance fluctuation into s-bits, we deploy a circuit consisting of six memtransistors ($MT1$, $MT2$, $MT3$, $MT4$, $MT5$, and $MT6$), as shown using the circuit diagram and corresponding optical image in Fig. 3d, e, respectively. The voltage waveforms applied to the nodes $N1$ and $N2$, i.e., V_{N1} and V_{N2}, respectively, are shown in Fig. 3f. Note that during each clock cycle (τ_{clk}), V_{N1} switches between 0 V, 0 V, and 2 V and V_{N2} switches between $V_P = -7$ V, $V_E = 10$ V, and $V_R = 1$ V. Voltages applied to nodes $N3$ and $N4$, i.e., V_{N3} and V_{N4}, are held constant at 1 V and 0 V, respectively. This allows programming and erasing of $MT1$ during each τ_{clk}. The voltage readout at node $N5$, i.e., V_{N5}, is shown in Fig. 3g and exhibits stochastic fluctuation. Note that the series connection of memtransistors $MT1$ and $MT2$ represents a voltage divider circuit, and hence V_{N5} is determined by their respective conductance values, i.e., G_{MT1} and G_{MT2}. Since G_{MT1} fluctuates from cycle-to-cycle owing to the programming and erasing voltages applied to its local back-gate terminal, i.e., $N2$, so does V_{N5}. In other words, the voltage divider translates conductance fluctuations into voltage fluctuations. Figure 3h shows the histogram of V_{N5}, which, as expected, follows a random Gaussian distribution with a mean (μ_{VN5}) of 0.40 V and standard deviation (σ_{VN5}) of 0.02 V.

Next, the Gaussian distribution is broadened by using an inverting amplifier constructed using $MT3$ and $MT4$. Note that the local back-gate of $MT3$ is shorted to its source at node N_6. This ensures that $MT3$ operates as a depletion mode (normally on) transistor or as a load resistor. Figure 3i shows the output, V_{N6}, as a function of the input, V_{N5}. The slope of the curve is referred to as the gain of the amplifier, and the higher the gain, the wider the broadening of the Gaussian. We achieved a gain of ~24. The gain can be increased further by cascading multiple amplifiers; however, this adds area and energy overhead. Figure 3j shows V_{N6} corresponding to V_{N5} obtained in Fig. 3g. Clearly, the histogram of V_{N6} shown in Fig. 3k exhibits a Gaussian distribution with a mean (μ_{VN6}) of 0.99 V and an increased standard deviation (σ_{VN6}) of 0.41 V.

Finally, to transform the analog fluctuations seen in V_{N6} into s-bits, a thresholding inverter with a programmable inversion threshold, V_{IT}, is constructed using $MT5$ and $MT6$. Figure 3l shows the output, V_{N7}, as a function of the input, V_{N6}, for different V_{IT}. Note that V_{IT} is the magnitude of V_{N6} for which V_{N7} reaches $V_{DD}/2$, i.e., 1 V in the present case. The programmability of V_{IT} is a critical feature that distinguishes 2D memtransistor-based inverters from conventional CMOS-based inverters and allows us to seamlessly obtain the s-bits. Figure 3m shows V_{N7} corresponding to V_{N6} obtained in Fig. 3j for different V_{IT} and Fig. 3n shows the corresponding probability of obtaining '1' in the bit-stream, i.e., p_s as a function of V_{IT}. As expected, if V_{IT} is too low, then almost all V_{N6} values translate into $V_{N7} \approx 0$ V, which is reflected as near zero p_s. Similarly, if V_{IT} is too high, then almost all V_{N6} values translate into $V_{N7} \approx 2$ V, leading to $p_s = 1$. Between these two extremes, p_s increases monotonically with V_{IT}. This clearly shows that we are able to convert the cycle-to-cycle random conductance fluctuations in 2D memtransistor into s-bits with reconfigurable p_s values that lie between [0,1] using the described circuit.

Note that the cycle-to-cycle variation in the programming of 2D memtransistors will lead to fluctuations in the threshold voltage (V_{TH}) of MT_6 and hence in V_{IT} of the thresholding inverter and p_s for the s-bit-stream. Supplementary Fig. S6a-b, respectively, show the distribution of V_{TH} and V_{IT} when MT_6 is subjected to 50 program/erase/read cycles with $V_P = -7$ V, $V_E = 10$ V, and $\tau_{P/E} = 100$ μs. The means and standard deviations were found to be −0.04 V and 0.08 V for V_{TH}, respectively, and 0.14 V and 0.08 V for V_{IT}, respectively. Therefore, p_s will not be perfectly deterministic; instead there will be a small uncertainty in its value, which is represented using the uncertainty band in Fig. 3n. Next, to assess randomness, we utilized the s-bit generator to generate 10^4 random bits using the same programming and erasing voltage pulses of $V_E = 10$ V and $V_P = -7$ V, respectively, at $\tau_{P/E} = 100$ μs. Supplementary Fig. S7 shows the results of eight of the statistical tests developed by the National Institute of Standards and Technology (NIST) performed on these 10^4 bits. According to the test protocol, the bit-streams are considered random only if the p-value is greater than 0.01 with the null hypothesis that the sequence is random with 99% confidence level. The NIST test results confirm that the s-bits generated are truly random.

The rough estimate of the energy expenditure for s-bit generation (E_{s-bit}) was calculated using Eq. (5).

$$E_{s-bit} = C_G\left(V_P^2 + V_E^2 + V_R^2 + V_{DD}^2\right) + \langle I_{N1N4}\rangle V_{DD}\tau_{clk} \tag{5}$$

$$\langle I_{N1N4}\rangle = \frac{1}{n}\sum_{i=1}^{n} I_{N1N4,i} \tag{6}$$

$$C_G = \varepsilon_0\varepsilon_{ox}WL/t_{ox} \tag{7}$$

In Eq. (5), V_P, V_E, V_R, and V_{DD} are the program, erase, read, and supply voltages, respectively. $C_G \approx 10^{-14}$ F is the gate capacitance, $\varepsilon_0 = 8.85\times10^{-12} F/m$ is the vacuum permittivity, and $\varepsilon_{ox} = 10$ and $t_{ox} = 50\,nm$ are, respectively, the relative permittivity and thickness of

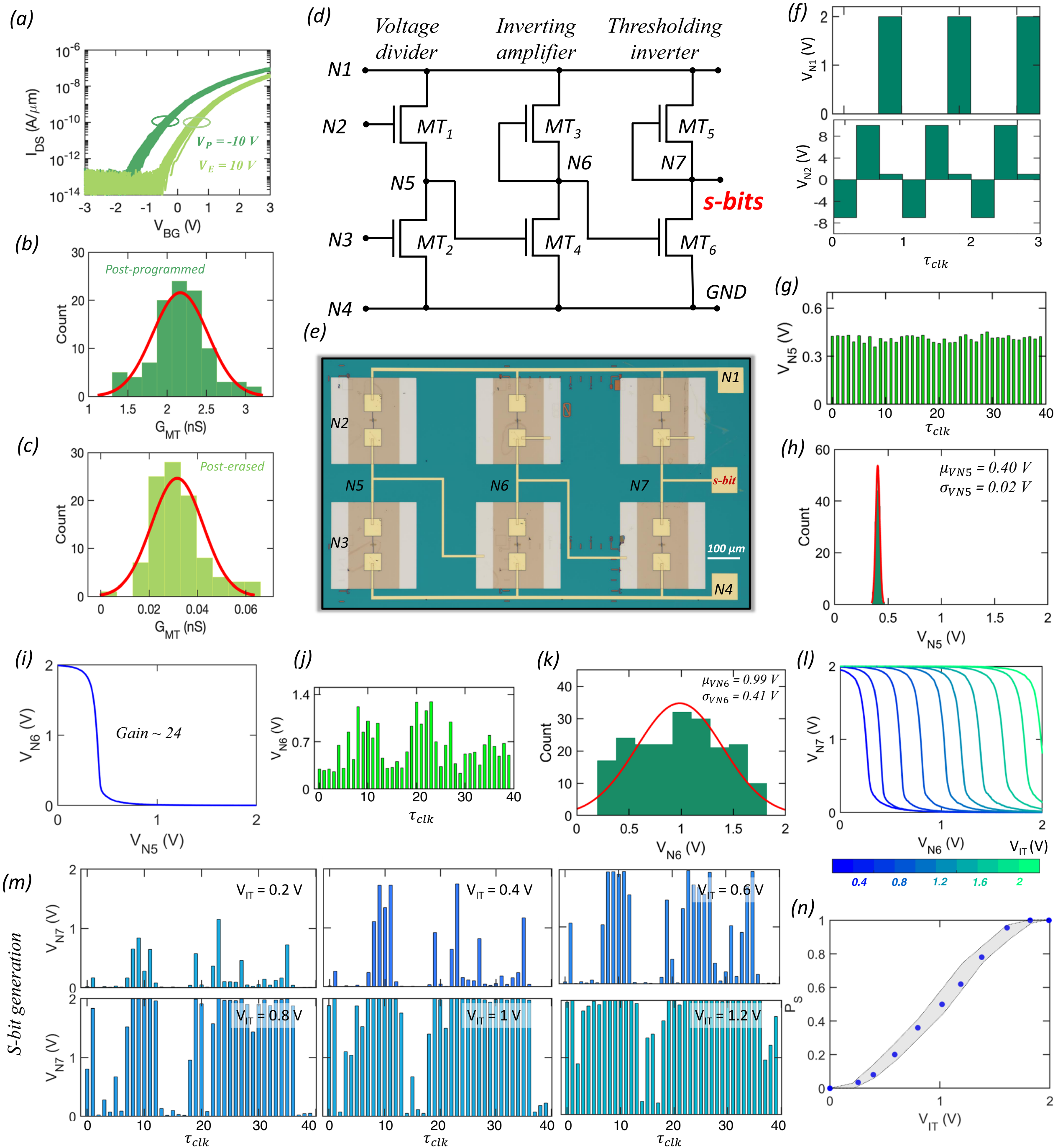

Fig. 3 | 2D memtransistor-based s-bit generator. **a** Transfer characteristics of a representative 2D memtransistor measured after the application of 100 cycles of V_P = −10 V (dark green) and V_E = 10 V (light green) pulses, each for τ_s = 100 μs. Distribution of **b** post-programmed and **c** post-erased conductance states (G_{MT}) measured using V_{BG} = 0 V. **d** Circuit diagram and **e** corresponding optical image for the proposed s-bit generator consisting of six memtransistors (*MT*1, *MT*2, *MT*3, *MT*4, *MT*5, *MT*6). **f** Voltage waveforms applied to nodes *N*1 and *N*2, i.e., V_{N1} and V_{N2}. During each clock cycle (τ_{clk}), V_{N1} toggles between 0 V, 0 V, and V_{DD} = 2 V and V_{N2} toggles between V_P = −7 V, V_E = 10 V, and V_R = 1 V. Voltages applied to nodes *N*3 and *N*4, i.e., V_{N3} and V_{N4}, are held constant at 1 V and 0 V, respectively. **g** Voltage readout at node *N*5, i.e., V_{N5}. **h** Distribution of V_{N5} over 200 τ_{clk} follows a random Gaussian distribution with a mean (μ_{VN5}) of 0.40 V and a standard deviation (σ_{VN5}) of 0.02 V. **i** Output, V_{N6}, of an inverting amplifier constructed using *MT*3 and *MT*4 as a function of the input, V_{N5}, with a gain of ~24. **j** V_{N6} corresponding to V_{N5} shown in **g**. **k** Distribution of V_{N6} follows a random Gaussian distribution with a mean (μ_{VN5}) of 0.99 V and a standard deviation (σ_{VN5}) of 0.41 V. **l** Output, V_{N7}, of a thresholding inverter constructed using *MT*5 and *MT*6 as a function of the input, V_{N6}, for different inversion threshold, V_{IT}. **m** V_{N7} corresponding to V_{N6} shown in **i** for different V_{IT}. **n** Probability of obtaining '1' in the bit-stream (p_s) as a function of V_{IT}.

Al_2O_3; W = 5 μm and L = 1 μm are, respectively, the channel width and length of the 2D-memtransistor. $\langle I_{N1N4} \rangle$ is the average current flowing through the s-bit generator circuit, i.e., the total current through the voltage divider, inverting amplifier, and threshold inverter during each τ_{clk}. We have used n = 200 to calculate the average current per τ_{clk} = 100 μs based on the experimental measurements. Since most of the memtransistors operate in their respective subthreshold regimes, the extracted $\langle I_{N1N4} \rangle$ is ~1.5 nA as shown in Supplementary Fig. S8. As such, the second term in Eq. (5) accounts for ~0.3 pJ, whereas the first term in Eq. (5) accounts for ~2 pJ. This results in $E_{s-bit} \approx$ 2 pJ/clock-cycle,

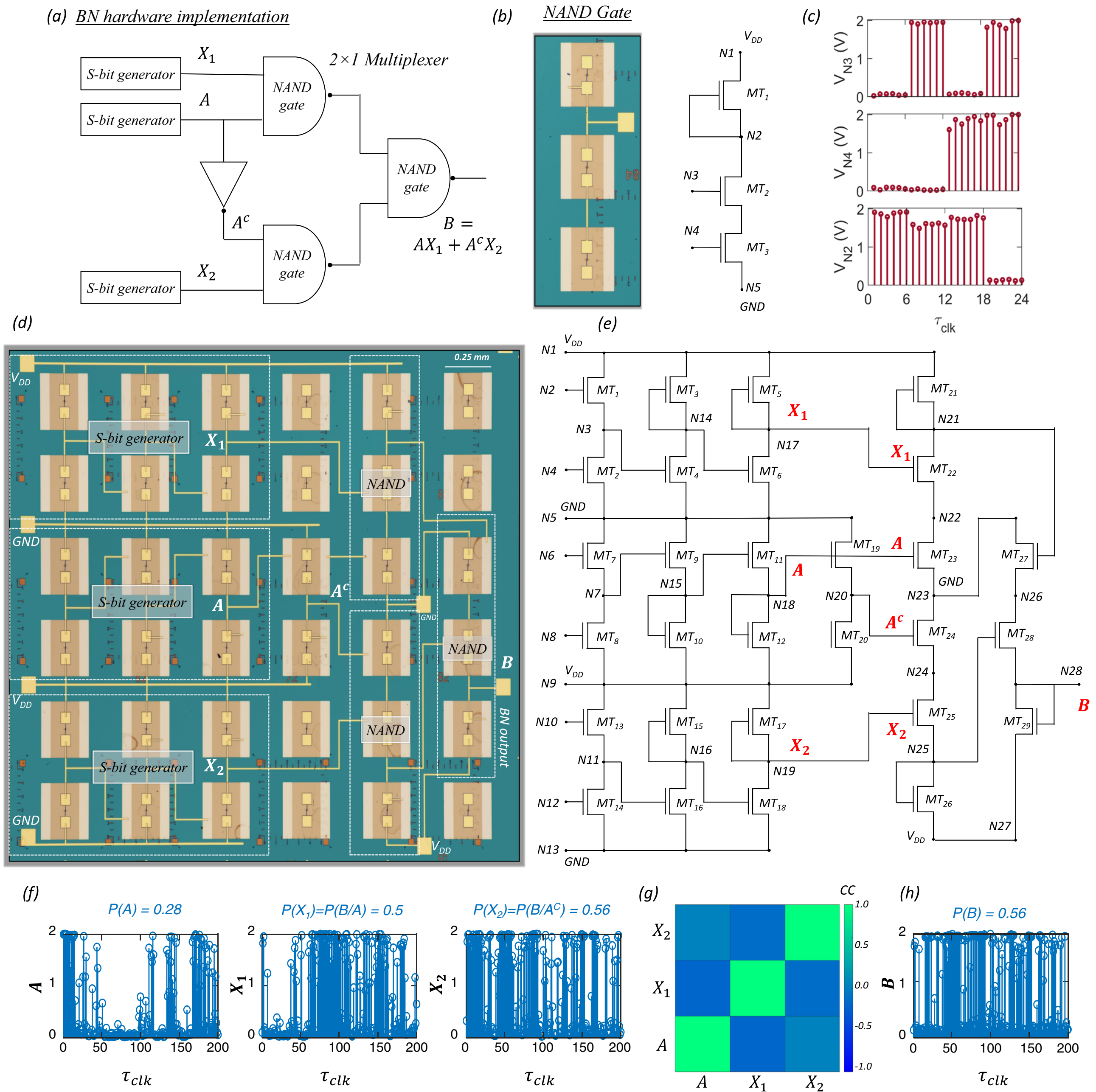

Fig. 4 | Hardware implementation of BN. a Circuit schematic for hardware implementation of a BN using three s-bit generators and one 2×1 *MUX*. The *MUX* consists of one inverter and three 2-input *NAND* gates. **b** Optical image and corresponding circuit configuration of a 2-input *NAND* gate comprising 3 memtransistors (*MT*1, *MT*2, and *MT*3) connected in series, with *MT*1 serving as the depletion load. **c** Input waveforms, V_{N3} and V_{N4}, which are applied to the local back-gate terminals of *MT*2 and *MT*3 at nodes N_3 and N_4, respectively, and the corresponding output waveform, V_{N2}, which is obtained at node N_2. **d** Optical image and **e** corresponding circuit configuration for hardware implementation of a 2-node BN consisting of 3 s-bit generators and a 2×1 *MUX* for a total of 29 memtransistors. The V_{IT} values for the s-bit generators for X_1 and X_2 can be preprogrammed using the CPT for the nodes A and B. **f** Representative stochastic bit-streams for the random variables A, X_1, and X_2 with $P(A) = 0.28$, $P(X_1) = P(B/A) = 0.50$, and $P(X_2) = P\left(B/A^C\right) = 0.56$. **g** Correlation coefficient (*CC*) values between A, X_1, and X_2 confirm mutual independence of the s-bit generator modules. **h** Stochastic bit-streams obtained at the output node, B. The measured and expected values for $P(B)$ are 0.56 and 0.54, respectively.

which supports our claim of energy efficient s-bit generation. Also note that since each memtransistor has an active device area of ~5 μm^2, excluding the large contact pads used for probing, the active footprint for the s-bit generator is ~30 μm^2. Since monolayer 2D materials offer aggressive dimensional scalability, it is possible to reduce the footprint of s-bit generators even further. Nevertheless, the use of only 6 memtransistors is the key towards the realization of area and energy efficient s-bit generator circuits.

2D memtransistor-based digital circuits and BN implementation

As described earlier, stochastic multiplexers (*MUX*s) can be used for computing the marginal probability values at any BN node. Figure 4a shows the circuit configuration of a 2×1 *MUX* which consists of one inverter and three 2-input *NAND* gates. Figure 4b shows the optical image and corresponding circuit configuration of a 2-input *NAND* gate comprising 3 memtransistors (*MT*1, *MT*2, and *MT*3) connected in series, with *MT*1 serving as the depletion load. The supply voltage,

V_{DD} = 2 V, is applied to the drain terminal of $MT1$ at node N_1, whereas the source terminal of $MT3$, i.e., node N_5, is kept grounded. Figure 4c shows the input waveforms, V_{N3} and V_{N4}, which are applied to the local back-gate terminals of $MT2$ and $MT3$ at nodes N_3 and N_4, respectively, and the corresponding output waveform, V_{N2}, which is obtained at node N_2. Clearly, the circuit operates as a *NAND* gate.

Figure 4d, e, respectively, show the optical image and corresponding circuit configuration for hardware implementation of a 2-node BN consisting of 3 s-bit generators and a 2 × 1 *MUX* for a total of 29 memtransistors. The V_{IT} values for the s-bit generators generating X_1 and X_2 can be pre-programmed corresponding to the CPT for the nodes *A* and *B* of the 2-node BN. Figure 4f shows the representative stochastic bit-streams for the random variables *A*, X_1, and X_2 with *P*(*A*) = 0.28, $P(X_1) = P(B/A)$ = 0.50, and $P(X_2) = P\left(B/A^C\right)$ = 0.56. Note that accurate estimation of *P*(*B*) requires that the stochastic input variables to the *MUX*, i.e., *A*, X_1, and X_2, must be mutually independent. Figure 4g shows the correlation coefficient (*CC*) between these three variables. The *CC* values were found to be close to zero, which confirms mutual independence of the s-bit generator modules. Figure 4h shows the stochastic bit-streams obtained at the output node, *B*. The measured and expected values for *P*(*B*) are 0.56 and 0.54, respectively. Supplementary Fig. S9 shows the results for three more sets of measurements. In all instances, we found that our 29 memtransistor module is able to demonstrate a 2-node BN with relatively high accuracy. The rough estimate of the energy expenditure for our hardware BN implementation is miniscule at ~1.2 nJ when 200 τ_{clk} are used. Certainly, the energy expense can be further reduced by shortening the length of the s-bit streams at the cost of reduced precision. Supplementary Fig. S10 shows the numerical simulation of the error in expected values for *P*(*B*) as a function of the bit-length of the s-bit stream for the inputs *P*(*A*), $P(B/A)$, and $P(B/A^C)$. The percentage error increases significantly with the reduction in bit-length of the s-bit streams.

While we have experimentally demonstrated that the distribution of the output voltage (V_{N6}) from the inverting amplifier follows a Gaussian profile, it is possible that the distribution may deviate from a perfect Gaussian distribution due to many operational reasons. This will definitely lead to computation error. To assess the impact of a skewed distribution on the precision of the BN, we have performed numerical simulations assuming that V_{N6} follows the Pearson random distribution function. Supplementary Fig. S11a shows the distribution of V_{N6} for different values of skewness from −1 to 1 in steps of 0.5. Note that a skewness of −1 or 1 will be a rare occurrence under most practical circumstances. Supplementary Fig. S11b shows the corresponding p_s as a function of V_{IT}. As the skewness increases, the deviation of p_s from its expected value also increases. Supplementary Fig. S11c shows the colormap of the percentage error in estimating *P*(*B*) using the BN hardware for different skewness in the stochastic input variables X_1 and X_2 that represent $P(B/A)$ and $P\left(B/A^C\right)$, respectively. As expected, the percentage error increases with increasing skewness. Furthermore, we have experimentally demonstrated that the distribution of the inverting threshold voltage (V_{IT}) exhibits a Gaussian distribution after $MT6$ is subjected to 50 program/erase/read cycles with V_P = −7 V, V_E = 10 V, and $\tau_{P/E}$ = 100 µs. This V_{IT} distribution leads to a small uncertainty ($\triangle P$) in probability of output voltages (V_{N7}), as shown in Fig. 3n. We have used numerical simulations to assess the impact of uncertainty in obtained probabilities on the precision of the BN, where the probability of the select line, *A*, remains as a constant while the probability of both X_1 and X_2 are inflicted with $\triangle P$ due to cycle-to-cycle variation in the programmed probability. Supplementary Fig. S12 shows the colormap of the percentage error in estimating *P*(*B*) using the BN hardware for uncertainty in the stochastic input variables X_1 and X_2 that represent $P(B/A) = 0.50$ and $P\left(B/A^C\right) = 0.56$, respectively, while $P(A) = 0.28$ and $\triangle P \approx 0.065$. From this colormap, we can conclude that even if the V_{IT} of the thresholding inverter ($MT6$) is inflicted with cycle-to-cycle variation from device programming, the inaccuracy of the 2-node Bayesian network ($B = AX_1 + A^C X_2$) is less than 15%. This simulation result shows decent accuracy in hardware implementation of the BN.

Finally, the impact of device-to-device variation on the operation of BN is examined. Supplementary Fig. S13a shows the transfer characteristics of 10 MoS_2 memtransistors and Supplementary Fig. S13b shows the transfer characteristics for these 10 devices after one programming/erasing clock cycle (V_P = −7 V, V_E = 10 V, and $\tau_{P/E}$ = 100 µs.). The device-to-device variation translates into error in $\triangle P$ and impacts the accuracy at the output of the BN. Supplementary Fig. S14 shows the colormap of error in *P*(*B*) for $P(X_1)$ = 0.5, $P(X_2)$ = 0.56, and *P*(*A*) = 0.28. We have used $\triangle P$ =0.046 for both X_1 and X_2 inferred from Supplementary Fig. S13b. From the error map, it is evident that the variation in the programmed probability inflicted by the device-to-device programming variation of the memtransistors resulted in a maximum error of 8% at the output of the BN.

Discussion

In conclusion, we have exploited cycle-to-cycle variability in the programmed conductance of 2D memtransistors and transcribed the same into s-bits with reconfigurable probability of obtaining '1' in the bit-stream using a circuit that comprises only 6 memtransistors and spends < 2 pJ per s-bit. We subsequently combined the s-bit generator with a 2D memtransistor-based 2 × 1 *MUX* to demonstrate hardware implementation of a BN. The BN architecture comprises 29 memtransistors and requires ~ 1.2 nJ of energy for precise computation. Our demonstration of a memtransistor-based standalone in-memory compute fabric shows the potential for emerging 2D materials and devices.

Methods

Fabrication of local back-gate islands

To define the back-gate island regions, a commercially-purchased substrate (285 nm SiO_2 on p^{++}-Si) was spin coated (4000 RPM for 45 s) with bilayer photoresist consisting of Lift-Off-Resist (LOR 5 A) and Series Photoresist (SPR 3012) and baked at 185 °C for 120 s and 95 °C for 60 s, respectively. The bilayer photoresist was then exposed using a Heidelburg Maskless Aligner (MLA 150) to define the island and developed using MF CD26 microposit, followed by a de-ionized (DI) water rinse. The back gate electrode of 20/50 nm TiN/Pt was deposited using reactive sputtering. The photoresist was removed using acetone and Photo Resist Stripper (PRS 3000) and cleaned using 2-propanol (IPA) and DI water. An atomic layer deposition (ALD) process was then implemented to grow 50 nm Al_2O_3 across the entire substrate, including the island regions. To access the individual Pt back-gate electrodes, etch patterns were defined using the same bilayer photoresist consisting of LOR 5 A and SPR 3012. The bilayer photoresist was then exposed to MLA 150 and developed using MF CD26 microposit. The 50 nm Al_2O_3 was subsequently dry etched using a BCl_3 reactive ion etch (RIE) chemistry at 5 °C for 20 s, which was repeated four times to minimize heating in the substrate. Finally, the photoresist was removed to give access to the individual Pt electrodes.

Large-area monolayer MoS_2 film growth

Monolayer MoS_2 was deposited on epi-ready 2″ c-sapphire substrate by metalorganic chemical vapor deposition (MOCVD). An inductively heated graphite susceptor equipped with wafer rotation in a cold-wall horizontal reactor was used to achieve uniform monolayer deposition as previously described[80]. Molybdenum hexacarbonyl ($Mo(CO)_6$) and hydrogen sulfide (H_2S) were used as precursors. $Mo(CO)_6$ maintained at 10 °C and 650 Torr in a stainless-steel bubbler was used to deliver 1.1×10^{-3} sccm of the metal precursor for the growth, while 400 sccm of H_2S was used for the process. MoS_2 deposition was carried out at

1000 °C and 50 Torr in H_2 ambient, where monolayer growth was achieved in 18 min. The substrate was first heated to 1000 °C in H_2 and maintained for 10 min before the growth was initiated. After growth, the substrate was cooled in H_2S to 300 °C to inhibit decomposition of the MoS_2 films. More details can be found in our earlier work[45, 48, 81].

MoS_2 film transfer to local back-gate islands

To fabricate the 2D memtransistors, the MOCVD-grown monolayer MoS_2 film was transferred from the sapphire growth substrate to the SiO_2/p^{++}-Si substrate with local back-gate islands using a PMMA (polymethyl-methacrylate) assisted wet transfer process. First, growth substrate was spin coated with PMMA and left to sit for 24 h to promote PMMA/MoS_2 adhesion. The corners of the spin-coated film were scratched using a razor blade and immersed inside 1 M NaOH solution kept at 90 °C. Capillary action caused the NaOH to be drawn into the substrate/film interface, separating the PMMA/MoS_2 film from the sapphire substrate. The separated film was rinsed three times inside separate water baths and fished-out using the SiO_2/p^{++}-Si substrate with local back-gate islands. The substrate was then baked at 50 °C and 70 °C for 10 min each to remove moisture and promote adhesion. An acetone bath was usd to remove the PMMA supporting layer, with a subsequent IPA bath to remove residue.

Fabrication of 2D memtransistors

To define the channel regions for the memtransistors, the substrate was spin-coated with PMMA and baked at 180 °C for 90 s. The resist was then patterned using electron beam (e-beam) lithography and developed using a 1:1 mixture of 4-methyl-2-pentanone (MIBK) and 2 propanol (IPA), with a subsequent IPA rinse. The monolayer MoS_2 film was then etched using a sulfur hexafluoride (SF_6) RIE chemistry at 5 °C for 30 s. Next, the sample was rinsed in acetone and IPA to remove PMMA. To define the source and drain contacts, sample was then spin coated with methyl methacrylate (MMA) followed by PMMA. E-beam lithography was used to pattern the source and drain contacts and 1:1 MIBK/ IPA was again used for development. 40 nm of nickel (Ni) and 30 nm of gold (Au) were deposited using e-beam evaporation. Finally, a lift-off process was performed to remove the excess Ni/Au and resist by immersing the sample in acetone for 30 min followed by IPA for another 30 mins. Each island contains one memtransistor to allow for individual gate control.

Monolithic integration

To define the connections between respective memtransistors, the substrate was spin coated with MMA and PMMA, followed by e-beam lithography and development using a 1:1 mixture of MIBK/IPA. E-beam evaporation of was used to deposit 60 nm of Ni and 30 nm of Au to form the connections. Finally, the e-beam resist was rinsed away by the same acetone and IPA lift-off process used previously.

Electrical characterization

Electrical characterization of the fabricated devices was performed using a Lake Shore CRX-VF probe station under atmospheric conditions and with Keysight B1500A parameter analyzer.

Data availability

The datasets generated during and/or analyzed during the current study are available from the corresponding author on reasonable request.

Code availability

The codes used for plotting the data are available from the corresponding authors on reasonable request.

References

1. Brown, G. E. & Smith, R. J. F. Conspecific skin extracts elicit anti-predator responses in juvenile rainbow trout (Oncorhynchus mykiss). *Can. J. Zool.* **75**, 1916–1922 (1997).
2. Puga, J. L., Krzywinski, M. & Altman, N. Bayesian networks. *Nat. Methods*. **12**, 799–800 (2015).
3. Smithson, S. C., Onizawa, N., Meyer, B. H., Gross, W. J. & Hanyu, T. Efficient CMOS Invertible Logic Using Stochastic Computing. *IEEE Trans. Circuits Syst. I: Regul. Pap.* **66**, 2263–2274 (2019).
4. Ardakani, A., Leduc-Primeau, F., Onizawa, N., Hanyu, T. & Gross, W. J. VLSI Implementation of Deep Neural Network Using Integral Stochastic Computing. *IEEE Trans. Very Large Scale Integr. (VLSI) Syst.* **25**, 2688–2699 (2017).
5. Alaghi, A. & Hayes, J. P. Survey of stochastic computing. *ACM Trans. Embedded Comput. Syst. (TECS)* **12**, 1–19 (2013).
6. Gaines, B. R. In *Proceedings of the April 18–20, 1967, spring joint computer conference*. 149–156.
7. Poppelbaum, W., Afuso, C. & Esch, J. In *Proceedings of the November 14–16, 1967, fall joint computer conference*. 635–644.
8. Weijia, Z., Ling, G. W. & Seng, Y. K. In *2007 IEEE Conference on Electron Devices and Solid-State Circuits*. 337–340.
9. Cai, R. et al. in *Proceedings of the Twenty-Third International Conference on Architectural Support for Programming Languages and Operating Systems* 476–488 (Association for Computing Machinery, Williamsburg, VA, USA, 2018).
10. Kulesza, Z. & Tylman, W. In *Proceedings of the International Conference Mixed Design of Integrated Circuits and System, 2006. MIXDES 2006*. 711-715.
11. Zermani, S., Dezan, C., Chenini, H., Diguet, J. & Euler, R. In *2015 IEEE Conference on Prognostics and Health Management (PHM)*. 1-10.
12. Knag, P., Lu, W. & Zhang, Z. A native stochastic computing architecture enabled by memristors. *IEEE Trans. Nanotechnol.* **13**, 283–293 (2014).
13. Gaba, S., Knag, P., Zhang, Z. & Lu, W. In *2014 IEEE International Symposium on Circuits and Systems (ISCAS)*. 2592-2595 (IEEE).
14. Gaba, S., Sheridan, P., Zhou, J., Choi, S. & Lu, W. Stochastic memristive devices for computing and neuromorphic applications. *Nanoscale* **5**, 5872–5878 (2013).
15. Debashis, P. *et al*. Hardware implementation of Bayesian network building blocks with stochastic spintronic devices. *Sci. Reports.* **10**, https://doi.org/10.1038/s41598-020-72842-6 (2020).
16. Faria, R., Kaiser, J., Camsari, K. Y. & Datta, S. Hardware Design for Autonomous Bayesian Networks. *Front. Computational Neurosci.* **15**, https://doi.org/10.3389/fncom.2021.584797 (2021).
17. Shim, Y., Chen, S., Sengupta, A. & Roy, K. Stochastic Spin-Orbit Torque Devices as Elements for Bayesian Inference. *Sci. Rep.* **7**, 14101 (2017).
18. Faria, R., Camsari, K. Y. & Datta, S. Implementing Bayesian networks with embedded stochastic MRAM. *AIP Adv.* **8**, 045101 (2018).
19. Venkatesan, R., Venkataramani, S., Fong, X., Roy, K. & Raghunathan, A. in *2015 Design, Automation & Test in Europe Conference & Exhibition (DATE)*. 1575–1578 (IEEE).
20. Finocchio, G. et al. The promise of spintronics for unconventional computing. *J. Magn. Magn. Mater.* **521**, 167506 (2021).
21. Hu, J., Li, B., Ma, C., Lilja, D. & Koester, S. J. Spin-Hall-Effect-Based Stochastic Number Generator for Parallel Stochastic Computing. *IEEE Trans. Electron Devices.* **66**, 3620–3627 (2019).
22. Yang, K. et al. In *2014 IEEE International Solid-State Circuits Conference Digest of Technical Papers (ISSCC)*. 280-281 (IEEE).
23. Pamula, V. R. et al. In *2018 IEEE Symposium on VLSI Circuits*. 1–2.
24. Satpathy, S. et al. In *2018 IEEE Symposium on VLSI Circuits*. 169–170.
25. Jayaraj, A., Gujarathi, N. N., Venkatesh, I. & Sanyal, A. 0.6–1.2 V, 0.22 pJ/bit True Random Number Generator Based on SAR ADC. *IEEE Trans. Circuits Syst. II: Express Briefs.* **67**, 1765–1769 (2020).

26. Bae, S., Kim, Y., Park, Y. & Kim, C. 3-Gb/s High-Speed True Random Number Generator Using Common-Mode Operating Comparator and Sampling Uncertainty of D Flip-Flop. *IEEE J. Solid-State Circuits*. **52**, 605–610 (2017).
27. Cao, Y., Zhao, X., Zheng, W., Zheng, Y. & Chang, C. H. A New Energy-Efficient and High Throughput Two-Phase Multi-Bit per Cycle Ring Oscillator-Based True Random Number Generator. *IEEE Trans. Circuits Syst. I: Regul. Pap.* **69**, 272–283 (2022).
28. Jaiswal, A., Fong, X. & Roy, K. Comprehensive scaling analysis of current induced switching in magnetic memories based on in-plane and perpendicular anisotropies. *IEEE J. Emerg. Sel. Top. Circuits Syst*. **6**, 120–133 (2016).
29. Sengupta, A., Panda, P., Wijesinghe, P., Kim, Y. & Roy, K. Magnetic tunnel junction mimics stochastic cortical spiking neurons. *Sci. Rep.* **6**, 1–8 (2016).
30. Daniels, M. W., Madhavan, A., Talatchian, P., Mizrahi, A. & Stiles, M. D. Energy-Efficient Stochastic Computing with Superparamagnetic Tunnel Junctions. *Phys. Rev. Appl*. **13**, 034016 (2020).
31. Vodenicarevic, D. et al. Low-Energy Truly Random Number Generation with Superparamagnetic Tunnel Junctions for Unconventional Computing. *Phys. Rev. Appl*. **8**, 054045 (2017).
32. Li, M.-Y., Su, S.-K., Wong, H.-S. P. & Li, L.-J. (Nature Publishing Group, 2019).
33. Jacob, A. P. et al. Scaling challenges for advanced CMOS devices. *Int. J. High. Speed Electron. Syst*. **26**, 1740001 (2017).
34. Uchida, K. et al. In *Digest. International Electron Devices Meeting*. 47–50 (IEEE).
35. Manzeli, S., Ovchinnikov, D., Pasquier, D., Yazyev, O. V. & Kis, A. 2D transition metal dichalcogenides. *Nat. Rev. Mater*. **2**, 17033 (2017).
36. Akinwande, D. et al. Graphene and two-dimensional materials for silicon technology. *Nature* **573**, 507–518 (2019).
37. Chhowalla, M., Jena, D. & Zhang, H. Two-dimensional semiconductors for transistors. *Nat. Rev. Mater*. **1**, 1–15 (2016).
38. Schwierz, F., Pezoldt, J. & Granzner, R. Two-dimensional materials and their prospects in transistor electronics. *Nanoscale* **7**, 8261–8283 (2015).
39. Liu, C. et al. Two-dimensional materials for next-generation computing technologies. *Nat. Nanotechnol*. **15**, 545–557 (2020).
40. Iannaccone, G., Bonaccorso, F., Colombo, L. & Fiori, G. Quantum engineering of transistors based on 2D materials heterostructures. *Nat. Nanotechnol*. **13**, 183–191 (2018).
41. Liu, Y. et al. Promises and prospects of two-dimensional transistors. *Nature* **591**, 43–53 (2021).
42. Shen, P.-C. et al. Ultralow contact resistance between semimetal and monolayer semiconductors. *Nature* **593**, 211–217 (2021).
43. English, C. D., Smithe, K. K. H., Xu, R. L. & Pop, E. In *2016 IEEE International Electron Devices Meeting (IEDM)*. 5.6.1-5.6.4.
44. Price, K. M., Schauble, K. E., McGuire, F. A., Farmer, D. B. & Franklin, A. D. Uniform Growth of Sub-5-Nanometer High-κ Dielectrics on MoS2 Using Plasma-Enhanced Atomic Layer Deposition. *ACS Appl. Mater. Interfaces*. **9**, 23072–23080 (2017).
45. Sebastian, A., Pendurthi, R., Choudhury, T. H., Redwing, J. M. & Das, S. Benchmarking monolayer MoS2 and WS2 field-effect transistors. *Nat. Commun*. **12**, 693 (2021).
46. Sebastian, A., Pannone, A., Subbulakshmi Radhakrishnan, S. & Das, S. Gaussian synapses for probabilistic neural networks. *Nat. Commun*. **10**, 4199 (2019).
47. Subbulakshmi Radhakrishnan, S., Sebastian, A., Oberoi, A., Das, S. & Das, S. A biomimetic neural encoder for spiking neural network. *Nat. Commun*. **12**, 2143 (2021).
48. Jayachandran, D. et al. A low-power biomimetic collision detector based on an in-memory molybdenum disulfide photodetector. *Nat. Electron.* **3**, 646–655 (2020).
49. Schranghamer, T. F., Oberoi, A. & Das, S. Graphene memristive synapses for high precision neuromorphic computing. *Nat. Commun.* **11**, 5474 (2020).
50. Das, S., Dodda, A. & Das, S. A biomimetic 2D transistor for audiomorphic computing. *Nat. Commun*. **10**, 3450 (2019).
51. Das, S. et al. Transistors based on two-dimensional materials for future integrated circuits. *Nat. Electron*. **4**, 786–799 (2021).
52. Zhu, K. et al. The development of integrated circuits based on two-dimensional materials. *Nat. Electron*. **4**, 775–785 (2021).
53. Wachter, S., Polyushkin, D. K., Bethge, O. & Mueller, T. A microprocessor based on a two-dimensional semiconductor. *Nat. Commun.* **8**, 14948 (2017).
54. Polyushkin, D. K. et al. Analogue two-dimensional semiconductor electronics. *Nat. Electron*. **3**, 486–491 (2020).
55. Nikonov, D. E. & Young, I. A. Benchmarking of beyond-CMOS exploratory devices for logic integrated circuits. *IEEE J. Exploratory Solid-State Computational Devices Circuits* **1**, 3–11 (2015).
56. Sylvia, S. S., Alam, K. & Lake, R. K. Uniform benchmarking of low-voltage van der Waals FETs. *IEEE J. Exploratory Solid-State Computational Devices Circuits* **2**, 28–35 (2016).
57. Lee, C.-S., Cline, B., Sinha, S., Yeric, G. & Wong, H. S. P. 32-bit Processor core at 5-nm technology: Analysis of transistor and interconnect impact on VLSI system performance. 28.23.21-28.23.24, https://doi.org/10.1109/iedm.2016.7838498 (2016).
58. Agarwal, T. et al. Benchmarking of monolithic 3D integrated MX_2 FETs with Si FinFETs. 5.7.1–5.7.4, https://doi.org/10.1109/iedm.2017.8268336 (2017).
59. 2DCC. *2d-crystal-consortium*, <https://www.mri.psu.edu/2d-crystal-consortium/user-facilities/thin-films/list-thin-film-samples-available>
60. Pendurthi, R. et al. Heterogeneous Integration of Atomically Thin Semiconductors for Non-von Neumann CMOS. *Small* **18**, 2202590 (2022).
61. Radhakrishnan, S. S. et al. A Sparse and Spike-timing-based Adaptive Photo Encoder for Augmenting Machine Vision for Spiking Neural Networks. *Adv. Materials*. 2202535 (2022).
62. Dodda, A., Trainor, N., Redwing, J. & Das, S. All-in-one, bio-inspired, and low-power crypto engines for near-sensor security based on two-dimensional memtransistors. *Nat. Commun*. **13**, 1–12 (2022).
63. Oberoi, A., Dodda, A., Liu, H., Terrones, M. & Das, S. Secure Electronics Enabled by Atomically Thin and Photosensitive Two-Dimensional Memtransistors. *ACS Nano*. **15**, 19815–19827 (2021).
64. Li, H. et al. From bulk to monolayer MoS2: evolution of Raman scattering. *Adv. Funct. Mater*. **22**, 1385–1390 (2012).
65. Das, S., Chen, H.-Y., Penumatcha, A. V. & Appenzeller, J. High performance multilayer MoS2 transistors with scandium contacts. *Nano Lett*. **13**, 100–105 (2013).
66. Schulman, D. S., Arnold, A. J. & Das, S. Contact engineering for 2D materials and devices. *Chem. Soc. Rev*. **47**, 3037–3058 (2018).
67. Chuang, S. et al. MoS2 p-type transistors and diodes enabled by high work function MoO x contacts. *Nano Lett*. **14**, 1337–1342 (2014).
68. Arnold, A. J. et al. Mimicking Neurotransmitter Release in Chemical Synapses via Hysteresis Engineering in MoS2 Transistors. *ACS Nano*. **11**, 3110–3118 (2017).
69. Illarionov, Y. Y. et al. The role of charge trapping in MoS_2/SiO_2 and MoS_2/hBN field-effect transistors. *2D Materials* **3**, https://doi.org/10.1088/2053–1583/3/3/035004 (2016).
70. Illarionov, Y. Y. et al. Energetic mapping of oxide traps in MoS2 field-effect transistors. *2D Mater*. **4**, 025108 (2017).
71. Jiang, J. et al. Defect engineering for modulating the trap states in 2D photoconductors. *Adv. Mater*. **30**, 1804332 (2018).
72. Tsai, H.-S. et al. Ultrafast exciton dynamics in scalable monolayer MoS2 synthesized by metal sulfurization. *ACS Omega*. **5**, 10725–10730 (2020).

73. Docherty, C. J. et al. Ultrafast transient terahertz conductivity of monolayer MoS2 and WSe2 grown by chemical vapor deposition. *ACS Nano*. **8**, 11147–11153 (2014).
74. Bhagdikar, S. & Mahapatra, S. In *2019 International Conference on Simulation of Semiconductor Processes and Devices (SISPAD)*. 1-4.
75. Grasser, T. Stochastic charge trapping in oxides: From random telegraph noise to bias temperature instabilities. *Microelectron. Reliab.* **52**, 39–70 (2012).
76. Waltl, M. In *2019 IEEE International Integrated Reliability Workshop (IIRW)*. 1-9.
77. Kirton, M. & Uren, M. Noise in solid-state microstructures: A new perspective on individual defects, interface states and low-frequency (1/*f*) noise. *Adv. Phys.* **38**, 367–468 (1989).
78. Ibe, O. *Markov processes for stochastic modeling*. (Newnes, 2013).
79. Uren, M., Kirton, M. & Collins, S. Anomalous telegraph noise in small-area silicon metal-oxide-semiconductor field-effect transistors. *Phys. Rev. B* **37**, 8346 (1988).
80. Xuan, Y. et al. Multi-scale modeling of gas-phase reactions in metal-organic chemical vapor deposition growth of WSe2. *J. Crys.Growth* **527**, https://doi.org/10.1016/j.jcrysgro.2019.125247 (2019).
81. Dodda, A. et al. Stochastic resonance in MoS2 photodetector. *Nat. Commun.* **11**, 4406 (2020).

Acknowledgements

The work was supported by Army Research Office (ARO) through Contract Number W911NF1920338 and National Science Foundation (NSF) through a CAREER Award under grant no. ECCS-2042154. Authors also acknowledge the materials support from the National Science Foundation (NSF) through the Pennsylvania State University 2D Crystal Consortium–Materials Innovation Platform (2DCCMIP) under NSF cooperative agreement DMR-2039351.

Author contributions

S.D. conceived the idea and designed the experiments. Y.Z., H.R., and T.F.S. fabricated the memtransistors. Y.Z., H.R., and S.D. performed the measurements, analyzed the data, discussed the results, and agreed on their implications. N.T. grew MOCVD MoS_2 under the supervision of J.M. R. All authors contributed to the preparation of the manuscript.

Competing interests

The authors declare no competing interests.

Additional information

Supplementary information The online version contains supplementary material available at https://doi.org/10.1038/s41467-022-33053-x.

Correspondence and requests for materials should be addressed to Saptarshi Das.

Peer review information *Nature Communications* thanks Punyashloka Debashis, Hyungjin Kim and the other, anonymous, reviewers for their contribution to the peer review of this work. Peer reviewer reports are available.

Reprints and permission information is available at http://www.nature.com/reprints

Publisher's note Springer Nature remains neutral with regard to jurisdictional claims in published maps and institutional affiliations.

Open Access This article is licensed under a Creative Commons Attribution 4.0 International License, which permits use, sharing, adaptation, distribution and reproduction in any medium or format, as long as you give appropriate credit to the original author(s) and the source, provide a link to the Creative Commons license, and indicate if changes were made. The images or other third party material in this article are included in the article's Creative Commons license, unless indicated otherwise in a credit line to the material. If material is not included in the article's Creative Commons license and your intended use is not permitted by statutory regulation or exceeds the permitted use, you will need to obtain permission directly from the copyright holder. To view a copy of this license, visit http://creativecommons.org/licenses/by/4.0/.

© The Author(s) 2022